Journal of Catalysis 456 (2026) 116774

Contents lists available at ScienceDirect

Journal of Catalysis

journal homepage: www.elsevier.com/locate/jcat

Research article

Mechanistic insights into the catalytic hydrogenation of furfural derivatives over Pd and Pt catalysts

Max Quayle, Zhuoli Wu, Marc Pera-Titus *, Alberto Roldan *

School of Chemistry, Cardiff Catalysis Institute, Cardiff University, Translational Research Hub, Maindy Road, Cardiff CF24 4HQ, UK

ARTICLE INFO

Keywords:
Hydrogenation
Catalysis
DFT
Furfural
Biomass

ABSTRACT

Furfural derivatives are promising bio-based platform molecules for the sustainable production of fuels and chemicals, yet their selective hydrogenation remains highly sensitive to catalyst choice. Here, we combine density functional theory (DFT) calculations with kinetic experiments to elucidate the mechanisms governing the hydrogenation of a furfural-derived α,β-unsaturated ketone, (E)-1-(furan-2-yl)-5-methylhex-1-en-3-one, over Pd and Pt catalysts. Periodic DFT calculations on Pd(111) and Pt(111) surfaces reveal low activation barriers for α-hydrogenation of the chain C=C bond on both metals, in agreement with the rapid and selective formation of the partially hydrogenated product observed experimentally. In contrast, hydrogenation of the furan ring is strongly metal-dependent. Over Pd(111), ring hydrogenation proceeds with relatively low barriers and limited charge accumulation on the ring carbons, enabling efficient conversion to the fully hydrogenated product. Over Pt(111), however, ring hydrogenation is associated with higher activation energies, significant positive charge accumulation, and weaker adsorption of hydrogenated ring intermediates.

Kinetic experiments over supported catalysts reveal distinct reaction regimes consistent with these predictions. While Pt catalysts exhibit transient formation of the fully hydrogenated product at early reaction times, the subsequent evolution of product yields is non-monotonic, reflecting reversible surface-mediated interconversion between partially and fully hydrogenated adsorbates in the presence of adsorbed hydrogen. At longer reaction times, secondary reactions further suppress net ring hydrogenation on Pt. Overall, this work demonstrates that charge redistribution and adsorption strength jointly control hydrogenation selectivity in furfural derivatives and provides mechanistic descriptors for the rational design of catalysts for biomass upgrading.

1. Introduction

Furfural derivatives have long been recognized as valuable intermediates owing to their renewable origin and versatile reactivity. Efficient synthetic routes for obtaining furfural from lignocellulosic waste have been available for nearly a century [1,2], making it an attractive precursor for manufacturing commodities, specialty chemicals, and fuels [3–10]. Furfural readily undergoes transformations involving its carbonyl group and furan ring, including Diels-Alder [11,12], Friedel-Crafts [13,14], and oxidation to maleic acid and its derivatives [15]. These reactions underpin its role as a precursor to numerous valuable compounds in the pharmaceutical [16,17] and agrochemical sectors [18]. The amenability of these compounds to oxidation and hydrogenation reactions has been readily exploited by organic chemists, leading to the development of industrial syntheses for valuable platform chemicals. Notable examples include tetrahydrofuran (a solvent and polymer precursor) [19–21], dimethylfuran (a high-octane biofuel) [22,23], 5-aminolevulinic acid (a biodegradable herbicide and medical imaging agent) [24–26], and 5-hydroxymethylfurfural (HMF), a versatile platform chemical with a litany of uses in the pharmaceutical and food industries [27–30]. Recent progress in bio-based polymer chemistry has further expanded the scope of furfural derivatives [31]. HMF can be readily oxidized to 2,5-furandicarboxylic acid (FDCA) [32,33], a renewable precursor to polyethylene terephthalate (PET) [34], while furfural can be oxidized to succinic acid [35,36]. Lomelí-Rodríguez *et al.* [37,38] developed FDCA-succinic acid biogenic copolymers for coatings. While PET remains the industry standard for the plastic packaging of soft drinks, FDCA can also undergo polycondensation to polyethylene furan-2,5-dicarboxylate (PEF) [39], a fully recyclable, heat-resistant plastic being investigated as an eco-friendly alternative to PET [40].

The aldol condensation reaction of furfural with a ketone, combined

* Corresponding authors.
E-mail addresses: peratitusm@cardiff.ac.uk (M. Pera-Titus), roldanmartineza@cardiff.ac.uk (A. Roldan).

https://doi.org/10.1016/j.jcat.2026.116774
Received 23 October 2025; Received in revised form 14 February 2026; Accepted 16 February 2026
Available online 17 February 2026

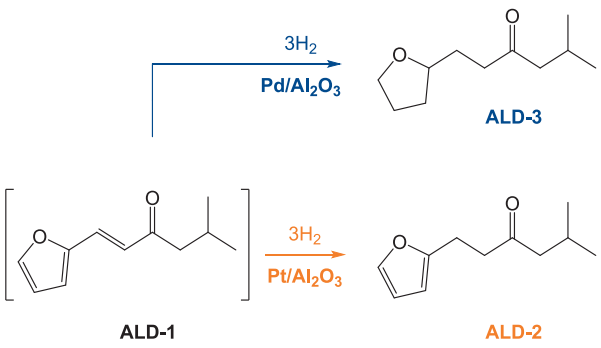

Scheme 1. The hydrogenation routes of ALD-1. Over Pt/Al_2O_3, the chain C=C bond is the only site that readily undergoes hydrogenation (ALD-2, orange), but over Pd/Al_2O_3, both the chain and ring sites are hydrogenated (ALD-3, blue) [42,49].

Table 1
Calculated adsorption energies of furfural and ALD-1 at the RPBE-D3(0) level against PBE and PBE-D3(0) values from the literature.

E_{ads}	Pd(111) (kJ mol^{-1})	Pt(111) (kJ mol^{-1})	References
Furfural, RPBE-D3(0)	–244.1	–101.3	This work
ALD-1, RPBE-D3(0)	–230.3	–179.5	This work
Furfural, PBE	–89.7	–102.3	[61]
Furfural, PBE-D3(0)	–190.1	–197.8	[61,62]
Furfural, experimental	–164.0	–56.0	[65,77]

with one or more sequential reactions (e.g. hydrogenation, reductive amination), has been proposed as a strategy to access biofuels, biosolvents, and biosurfactants with controllable carbon molecular weight [23,41,42]. These transformations require two or more steps that can be carried out either in sequential catalytic reactors or in a single reactor in a one-pot fashion, combining different catalysts or a multi-site catalyst, avoiding the separation of intermediates and reducing waste. Sequential [8,43–45] and one-pot [5,10,46,47] reactions have been developed targeting the synthesis of branched alkanes as jet fuels and monomers for polyester and epoxy resins, starting from the aldol condensation reaction of furfural with a ketone, followed by hydrodeoxygenation (HDO) at solvent-free conditions.

One-pot reactions have been reported for manufacturing furan- and THF-derived alcohols and amines by the aldol condensation/crotonization reaction of furfural with ketones, followed by hydrogenation with H_2 [3,6,9] or reductive amination with NH_3 and H_2, respectively [42,48]. For instance, the ketone (*E*)-1-(furan-2-yl)-5-methylhex-1-en-3-one (ALD-1) can be synthesized directly from furfural by the aldol condensation/crotonization with methyl isobutyl ketone (MIBK). As shown in Scheme 1, the hydrogenation of ALD-1′s conjugated ring system proved to be highly selective [42,49]. The C=C double bond on the branching chain of ALD-1 was reduced over both Pd and Pt, generating ALD-2. However, subsequent hydrogenation of ALD-2′s ring system to ALD-3 was catalyst dependent. Over Pd, catalysis proved to be highly selective towards ALD-3. Even at temperatures as mild as 80 °C, the furan ring was fully hydrogenated, with conversion reaching 100% within hours. Over Pt, meanwhile, catalytic activity and selectivity towards ALD-3 was poor, resulting in ALD-2 being the dominant product.

To rationalize the divergent catalytic behavior of Pd and Pt catalysts towards hydrogenation of the furan ring of ALD-1, we constructed thermodynamic and kinetic energy profiles of all possible ALD-1 hydrogenation paths over periodic slab models of Pd(111) and Pt(111); facets that have been shown experimentally [50–52] and computationally [53,54] to be particularly active for hydrogenation. A Langmuir-Hinshelwood type mechanism was assumed based on the experimental observations of hydrogenation over the transition metal catalysts [55–57]. Intermediates were generated for each product by reducing the substrate with one H atom at a time to ensure the

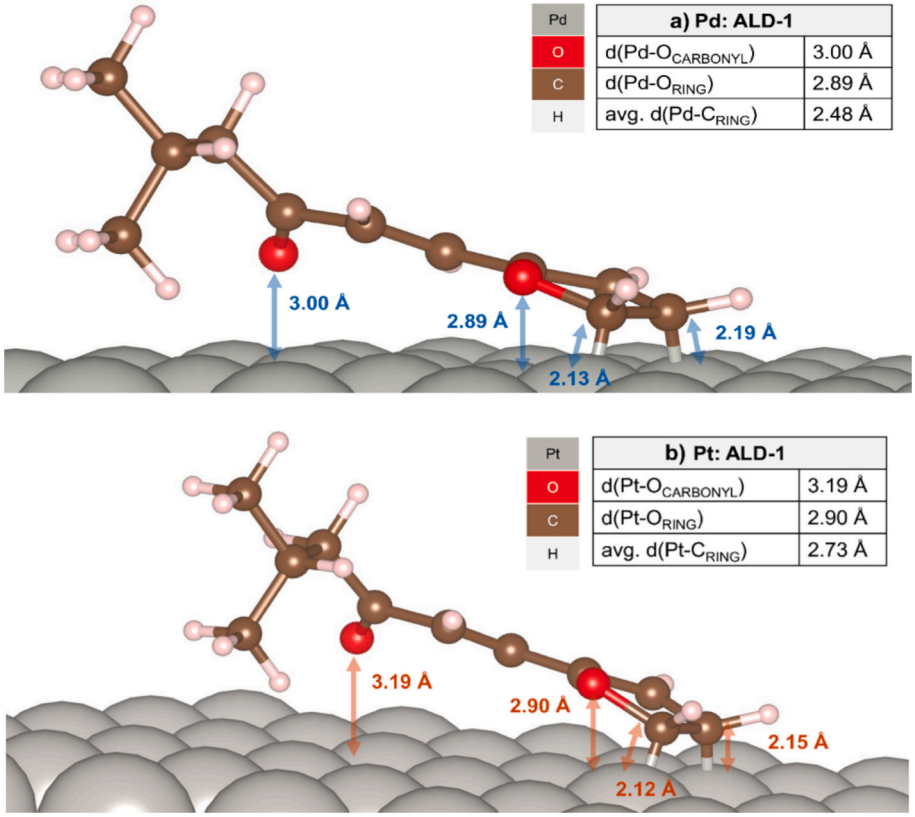

Fig. 1. Binding conformations of ALD-1 over (a) Pd(111) and (b) Pt(111).

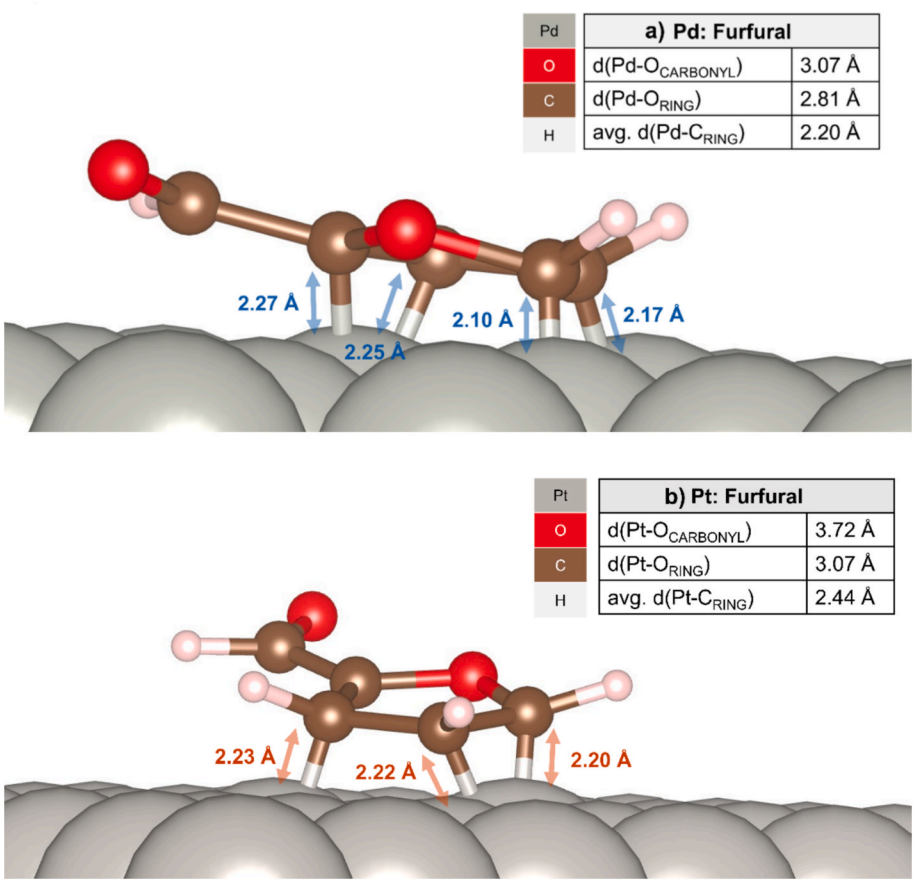

Fig. 2. Binding conformations of furfural over (a) Pd(111) and (b) Pt(111).

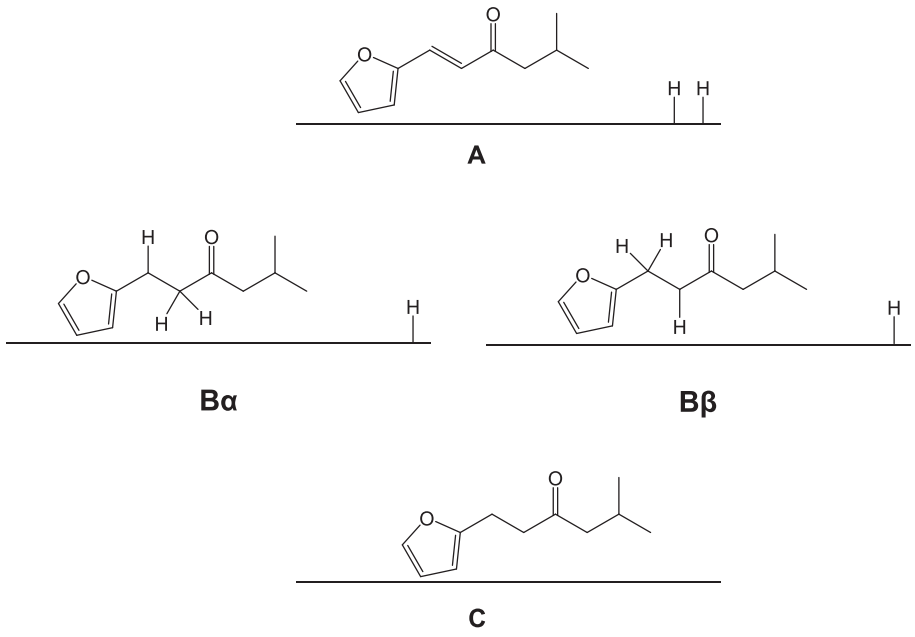

Scheme 2. Schematic representation of the intermediates associated with the chain hydrogenation of ALD-1 to ALD-2.

construction of a systematic and physically accurate picture of the reaction profile.

2. Methods

2.1. Computational details

Density functional theory (DFT) models of all possible ALD-1

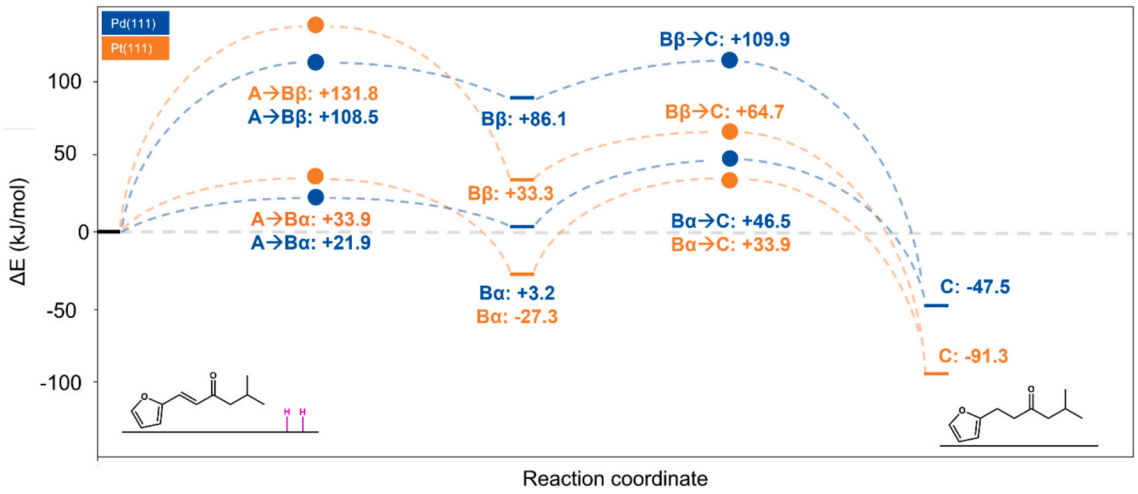

Fig. 3. The energy profile for the chain hydrogenation of ALD-1 over Pd(111) (blue) and Pt(111) (orange). Transition states between minima are marked with colored circles. Insets are the schematic representations of ALD-1 co-adsorbed with two H adatoms (left) and adsorbed ALD-2 (right). (For interpretation of the references to colour in this figure legend, the reader is referred to the web version of this article.)

hydrogenation intermediates over Pd(111) and Pt(111) were calculated using the Vienna Ab-Initio Simulation Package (VASP) [58] under the constraints of the generalized gradient approximation (GGA) at the RPBE-D3(0) level [59,60]. In line with previous computational studies of furfural adsorption [61,62], the zero-damping D3 correction (D3(0)) of Grimme *et al.* [60] led to mild overbinding for both Pd(111) and Pt (111). While furfural's conformational geometry was effectively unchanged by introducing the dispersion correction, the same cannot be said about the energetics of the transition states associated with hydrogenation, which can be modelled to a far higher degree of accuracy with the inclusion of D3(0) [60,61,63,64]. In addition, the model neglects solvation effects, although as reported by Yu *et al.* in their experimental study of Pd-catalyzed furfural hydrogenation [65], stabilizing solvation effects from neighboring hydronium ions can decrease furfural's enthalpy of adsorption by as much as 100 kJ mol^{-1}. As both furfural and ALD-1 are experimentally known to readily adsorb to both metals [42,61] and the geometry of adsorbates remained effectively unchanged when D3(0) dispersion corrections were introduced into our calculations, we kept them at the compromise of over-binding, thus ensuring that the activation energy barriers for all reactions on the surface were as accurate as possible.

The Brillouin zone was sampled with a 3 × 3 × 1 Monkhorst-Pack mesh [66]. All atoms were modelled using projector augmented wave (PAW) potentials [67,68]. The plane-wave cutoff energy was set to 500 eV, the ionic convergence threshold to 0.03 eV/Å, and the electronic convergence threshold to 1×10^{-5} eV. Catalyst surfaces were modeled as $p(6 \times 6 \times 6)$ slabs separated by a 15 Å vacuum layer along the z-axis. To improve convergence, the bottom three layers were frozen at the bulk-optimized lattice, and both lateral interactions and coverage effects were neglected due to the size of ALD-1 and its derivatives. Due to its strong performance in prior reviews of charge partition schemes [69,70], net atomic charges were calculated *via* DDEC6 population analysis on the optimized structures, as implemented in CHARGEMOL [71–74].

Transition states associated with each hydrogenation step were identified using the improved dimer method [75,76]. Initial guess structures were constructed by linearly interpolating the positions of the atoms from the coordinates of the optimized intermediates. These structures were then subjected to vibrational analysis to identify the dimer axis, a vector along the potential energy surface (PES) corresponding to an imaginary vibration mode associated with the transition state. Constrained optimization was carried out along the dimer axis until a transition state was identified with a trial step size of ±0.01 Å. All optimized structures were then subjected to a second round of vibrational analysis to confirm the presence of a single order saddle point on the PES. Adsorption energies (E_{ads}) of the surface species were calculated as follows:

$$E_{ads} = E_{X^*} - E_* - E_X \quad (1)$$

where E_{X^*} is the ground state energy of species X bound to the surface, E_* is the ground state energy of the naked surface, and E_X is the ground state energy of X in the gas phase.

2.2. Experimental details

2.2.1. Materials

Furfural (99%), methyl isobutyl ketone (MIBK) (≥98.5%), and Amberlyst® A26 Ion Exchange resin (16–50 mesh), and 5%Pd/Al_2O_3 (103 m^2/g), 5%Pt/Al_2O_3 (108 m^2/g), 5%Pd/C (898 m^2/g), and 5%Pt/C (800 m^2/g) catalysts were supplied by Sigma Aldrich. H_2 (99.99%) was procured from British Oxygen Company).

2.2.2. Synthesis of ALD-1

In order to obtain the substrate (*E*)-1-(furan-2-yl)-4-methylpent-1-en-3-on (ALD-1), furfural (10.4 mmol), and MIBK (100.0 mmol) were reacted over A26 at 120 °C for 2 h in a 35 mL sealed glass reactor tube. Excess MIBK was removed by rotary evaporation, giving (*E*)-1-(furan-2-yl)-4-methylpent-1-en-3-one (ALD-1) with 96% yield. The purity measured by gas chromatography was 97.5%.

2.2.3. Catalytic hydrogenation tests

ALD-1 hydrogenation over Pd/Al_2O_3 or Pt/Al_2O_3 catalysts was carried out in a 50 mL stainless steel autoclave (DG Innovative Engineering Design Solutions). Before the tests, the catalysts were reduced at 200 °C in a H_2/Ar atmosphere for 4 h. At the start of each test, the catalyst (66 mg), ALD-1 (3.2 mmol), and MIBK (59.3 mmol) were added to the autoclave. The reactor mixture was flushed with H_2 and pressurized to 20 bar at room temperature. The mixture was then heated to 180 °C and the reaction was conducted at variable times (from 1 to 18 h) under magnetic stirring (800 rpm). After each run, the reactor was depressurized, cooled to room temperature, and the catalyst was removed by centrifugation. The unconverted reactants and products were analyzed by gas chromatography using an Agilent 7890A GC equipped with a CP-Wax 52 C8 column and a flame ionization detector (FID). The column was programmed with a 3 °C·min^{-1} initial ramp from 80 °C to 100 °C, followed by a 50 °C·min^{-1} ramp to 300 °C, holding this temperature for

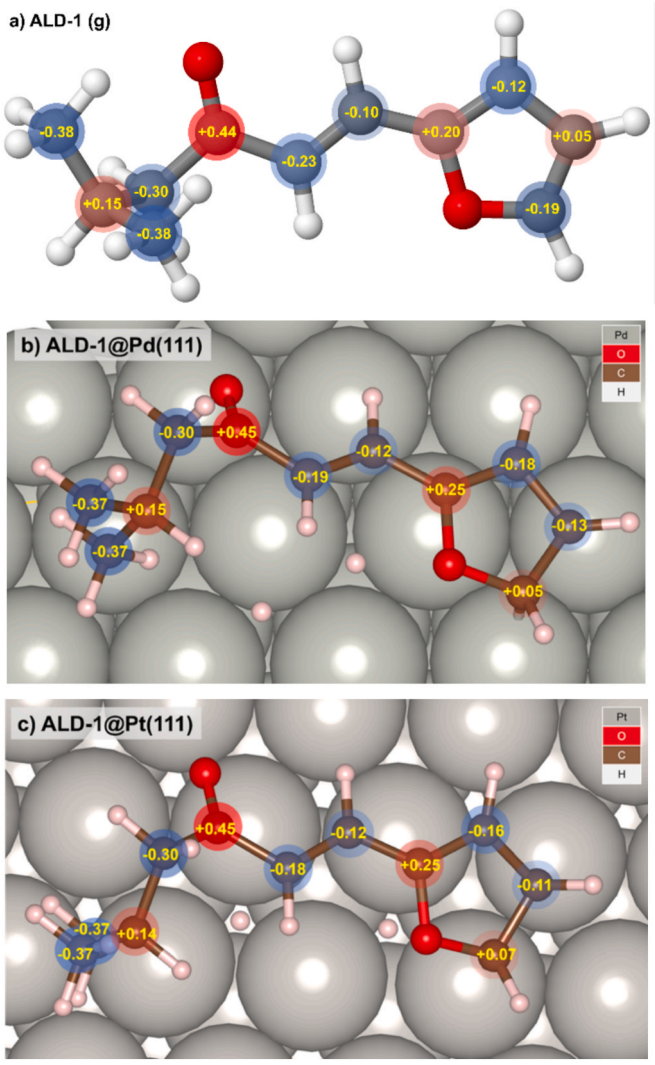

Fig. 4. DDEC6 charge analysis of ALD-1 (a) in the gas phase and adsorbed to (b) Pd(111) and (c) Pt(111). Carbon atoms with partial positive and negative charges are highlighted in red and blue, respectively. Inset charge values are given in units of $|e^-|$. (For interpretation of the references to colour in this figure legend, the reader is referred to the web version of this article.)

3 min. The ALD-1 conversion, selectivity, yield, carbon balance, and catalytic activity were calculated as follows:

$$\text{ALD-1 conversion } (\%) = \left(1 - \frac{n_{ALD-1}}{n^0_{ALD-1}}\right) x100 \quad (2)$$

$$\text{Selectivity}_i\ (\%) = \left(\frac{n_i}{n^0_{ALD-1} - n_{ALD-1}}\right) x100 \quad (3)$$

$$\text{Yield}_i\ (\%) = \left(\frac{n_i}{n^0_{ALD-1}}\right) x100 \quad (4)$$

$$\text{Carbon loss } (\%) = \left(1 - \frac{n_{ALD-1}}{n^0_{ALD-1}} - \frac{\sum_i n_i}{n^0_{ALD-1}}\right) x100 \quad (5)$$

where n^0_{ALD-1} and n_{ALD-1} refer to the initial and final number of moles of ALD-1, n_i is the number of moles of the i^{th} product, and m_{cat} is the catalyst loading. The ALD-1 conversion and selectivity to the different products were reproducible to within 5%.

Formation of by-products was investigated using gas chromatography-mass spectrometry (GC–MS) on a Q Exactive GC Orbitrap GC–MS/MS (ThermoFisher) instrument (Source Type ESI, Scan Begin 50 *m/z*, Scan End 1000 *m/z*, Ion Polarity Positive) equipped with a TG5 SILMS 30 m Column.

2.2.4. Catalyst characterization

ICP analysis and samples preparation. After weighing, samples were digested with 5 mL reverse aqua regia in an *Analytix Ethos Up* microwave system, with procedural blanks included. Digests were diluted to 50 mL with ultrapure water. Prior to measurement, digests were typically diluted 50-fold to bring analyte concentrations within the calibration range. Elemental quantification was performed on an *Agilent 7900 ICP-MS* operated in standard and single-particle (spICP-MS) modes. Calibration was achieved using a six-point curve prepared from certified reference materials in 2% HNO_3 and 1% HCl (v/v). A certified internal standard was continuously introduced online to correct for instrumental drift and matrix effects.

Temperature-programmed reduction (H_2-TPR). The reducibility of the catalysts was measured by H_2-TPR on a Micromeritics AutoChem II 2920 system equipped with a thermal conductivity detector (TCD) to monitor changes in gas composition. The H_2-TPR profiles were measured from 30 to 900 °C at a heating rate of 10 °C/min under a 5% H_2/Ar flow (40 mL (STP)/min).

Thermogravimetric Analysis (TGA). Thermogravimetric measurements were performed in a Thermal Analysis System TGA 4000 from PerkinElmer equipped with a dynamic gas system. The sample (approx. 40 mg) was placed in an open alumina crucible and heated up to 800 °C (5 °C·min^{-1}) under a nitrogen atmosphere with a gas flow of 50 mL·min^{-1}.

Transmission Electron Microscopy (TEM). The Pt/Pd distribution on alumina and carbon supports were inspected by high-resolution transmission electron microscopy (HR-TEM) using a JEOL 2100-JEM microscope at a 200 kV accelerating voltage. ImageJ software was used to measure the average size of Pd and Pt nanoparticles on both catalysts from particle size distributions using 150 nanoparticles. The metal dispersion, D, was measured from the average particle sizes using the expression

$$D(\%) = 6\frac{M_i}{\rho_i}\frac{1}{N_A \pi r_i^2}\frac{1}{d_p} \quad (6)$$

where ρ_i is the metal density, N_A is the Avogadro Number, r_i is the covalent radius of the metal and d_p is the average size of metal nanoparticles measured by TEM, assuming spherical shape.

3. Results and discussion

3.1. Chain hydrogenation

Conformational analysis (Table 1) showed that ALD-1 adopted a similar binding conformation over Pd(111) and Pt(111) through its ring (Fig. 1) in a manner reminiscent of furfural (Fig. 2), with the alkyl chain positioning itself away from the surface.

In the present work, ALD-1 was deliberately evaluated under gas-phase, low-coverage conditions to isolate the fundamental adsorption strength that governs initial adsorption and final desorption barriers in vapour-phase reaction cycles. This means that the calculated adsorption energies may be slightly overestimated compared to experimental results, such as calorimetric studies by Campbell and co-workers [78], which demonstrate that the presence of water or other co-adsorbates can significantly weaken the apparent adsorption energies of organic molecules on metal surfaces through competitive adsorption and solvent-induced destabilization.

The labels and structures of the intermediates in the chain hydrogenation process are given in Scheme 2. ALD-1 hydrogenation can occur at four possible sites: the chain C═C bond, the carbonyl group, and the two C═C bonds of the furan ring system. Henceforth, we will refer to the C2═C3 and C4═C5 bonds as the ortho and para hydrogenation sites,

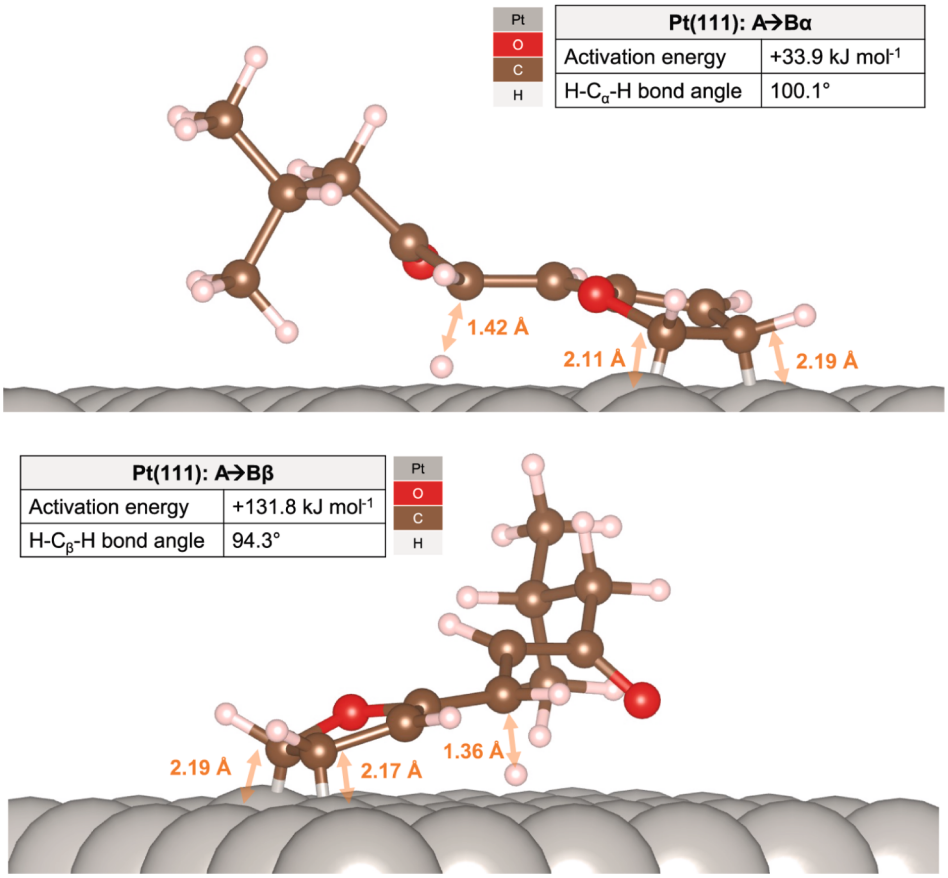

Fig. 5. Schematic representation of the optimized transition state structures for the initial chain hydrogenation through the α- and β-carbon over Pt(111).

respectively, in the remainder of this study.

The experimental work of Gao *et al.* [49] showed that ALD-1 hydrogenation proceeds first at the double bond of the acrylic group in the chain. This hydrogenation also occurred preferentially in the presence of ammonia [41]. Consequently, this bond was the first to be considered in our analysis. As shown in Fig. 3, the total activation energy barriers for chain hydrogenation over Pd(111) (E_A = +46.5 kJ mol^{-1}) and Pt(111) (E_A = +33.9 kJ mol^{-1}) are both low and close to one another. The activation energy barriers for β-hydrogenation over both Pd(111) (E_A = +109.9 kJ mol^{-1}) and Pt(111) (E_A = +131.8 kJ mol^{-1}) are more than twice as large as the corresponding barriers for α-hydrogenation. Comparison of the activation energies results in kinetically favorable chain hydrogenation in agreement with experimental observations.

The computational work of Jia et al. [79] on the hydrogenation of acrylates found that α-hydrogenation is driven by the distribution of partial charges across the molecule. DDEC6 population analysis of ALD-1 in the gas phase confirmed this (Fig. 4a). Due to its vicinity to a partially positive C═O carbon (q = +0.44 e), electron density accumulates at the α-carbon (q = –0.23 e) to prevent the formation of a localized positive charge on the chain. When ALD-1 binds to the catalyst through its ring system, this buildup in electron density at the α-carbon likely facilitates hydrogenation by H adatoms from the surface. To assess this hypothesis, a second round of DDEC6 population analysis was conducted on ALD-1 adsorbed to Pd(111) and Pt(111). As shown in Fig. 4ab and c, the charge discrepancy between the vinyl carbons is preserved over both Pd(111) and Pt(111). The localized negative charge on the α-carbon was preserved over both catalysts, which strongly suggests that the selectivity towards α-hydrogenation over Pd(111) and Pt(111) is driven by the distribution of charge across the C═C bond.

To determine the stability of radical intermediates, spin-polarized single point energy calculations were conducted on the optimized Bα and Bβ structures. The magnetic moments of the Bα adsorbate atoms were negligible ($m < 0.005\ \mu_B$) over both Pd(111) and Pt(111). While a small magnetic moment of 0.042 μ_B was observed on the α-carbon of the A → Bβ transition state over Pd(111), significant delocalization of an unpaired electron was observed over Pt(111) between the α-carbon (m = 0.351 μ_B) and the oxygen of the carbonyl group (m = 0.182 μ_B). Although the ease with which radical species can delocalize likely contributes to the marked stability of the Bβ intermediate over Pt(111), the absence of intermediates with radical character along the α-hydrogenation pathway suggests that charge distribution is a stronger predictor of selectivity than radical stability.

In addition to being favored by the distribution of negative charge across ALD-1, α-hydrogenation benefits from sterically favorable transition states. This is illustrated by the optimized transition states corresponding to the A → Bα and the A → Bβ steps over Pt(111) (Fig. 5, Table S1). While the interatomic distances between the carbon and the migratory H atom are similar in both cases, the α-carbon can adopt a favorable bond formation with an angle of 100.1°. In contrast, hydrogenation can only be initiated at the β-carbon through an unfavorable bond formation angle of 94.3°. While this barrier may be surmountable at high temperatures, it is likely that an α-hydrogenation mechanism dominates regardless of whether a Pd or Pt catalyst is used.

3.2. *Ring hydrogenation*

A comprehensive schematic of the intermediates associated with ring hydrogenation is provided in Scheme 3. A complete list of intermediate energies and activation energy barriers is provided in Table S2, which leads to the reaction profile for ortho hydrogenation, as shown in Fig. 6. The activation energy for ring hydrogenation is substantially lower over Pd(111) (+69.1 kJ mol^{-1}) than over Pt(111) (+114.0 kJ mol^{-1}). In both

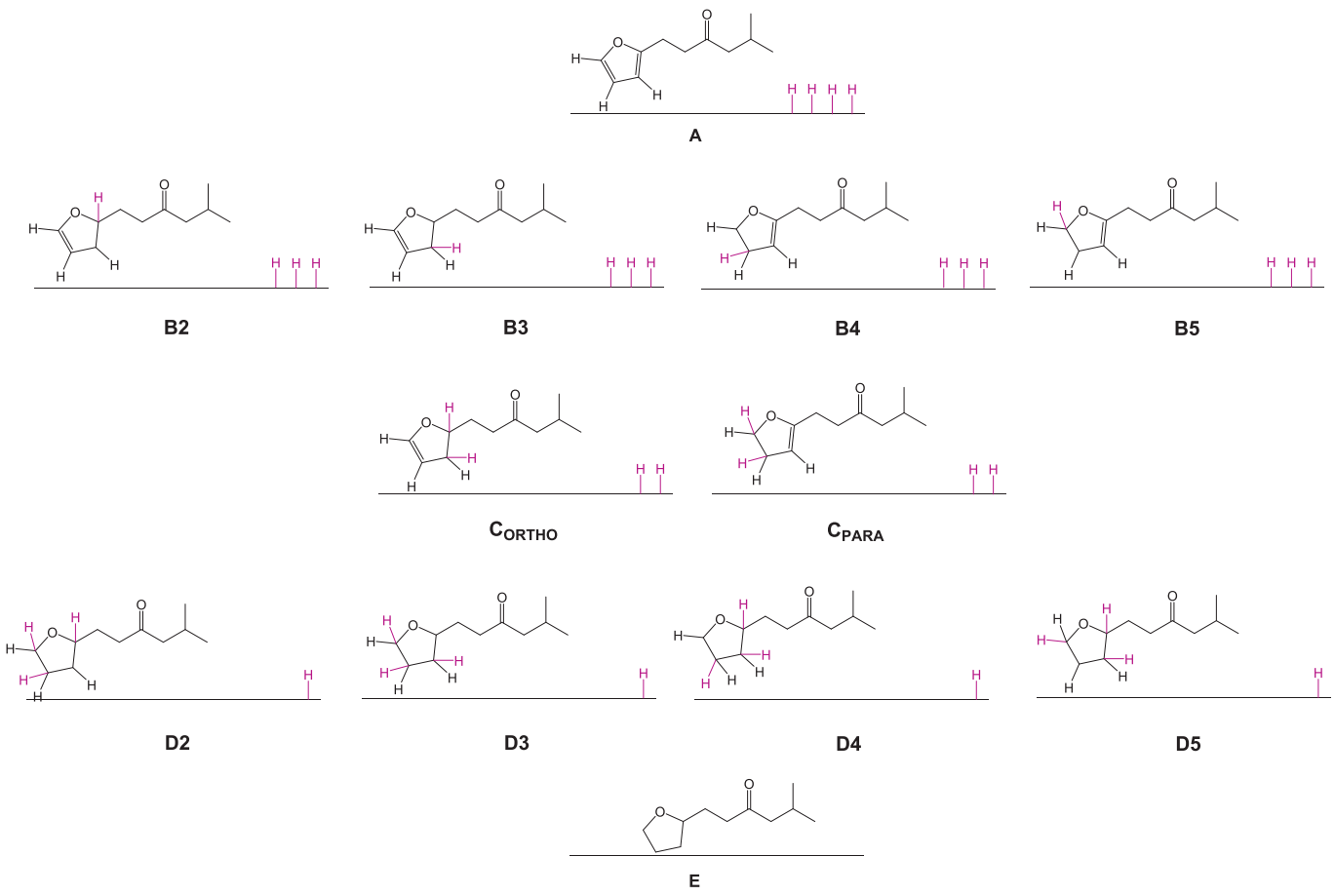

Scheme 3. Intermediates associated with ring hydrogenation. H adatoms from dissociated H_2 are highlighted in pink.

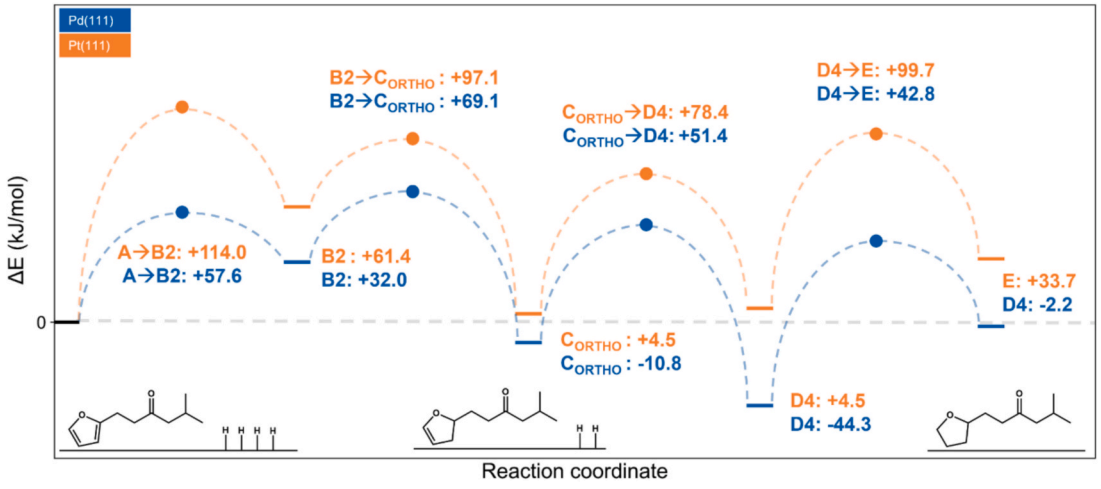

Fig. 6. Energy profile for *ortho* hydrogenation of ALD-2 over Pd(111) (blue) and Pt(111) (orange). Transition states between minima are marked with colored circles. Inset are the schematic representations of ALD-2 co-adsorbed with four H adatoms (left) and adsorbed ALD-3 (right). Relative energies are in kJ/mol. (For interpretation of the references to colour in this figure legend, the reader is referred to the web version of this article.)

cases, the *ortho* hydrogenation is energetically favored over the *para* hydrogenation. The preferred order of hydrogenation is B2, then C_{ORTHO}, then D4, then E.

A profile depicting the minimum energy path associated with *para* hydrogenation is provided in Fig. 7. As with *ortho* hydrogenation, the optimal order of carbon hydrogenation is identical regardless of the catalyst: B5, then C_{PARA}, then D3, then E. The activation energy for *para* hydrogenation over Pd(111) (E_A = +96.1 kJ mol^{-1}) is almost 40% higher than the corresponding value for *ortho* hydrogenation. While the energy difference between the routes is relatively large, it is plausible that Pd-catalyzed *para* hydrogenation could compete with *ortho* hydrogenation at the experimental operating temperature of 180 °C.

The large energy barrier associated with *para* hydrogenation over Pt(111) (+208.3 kJ mol^{-1}) is likely insurmountable at 180 °C. It should be

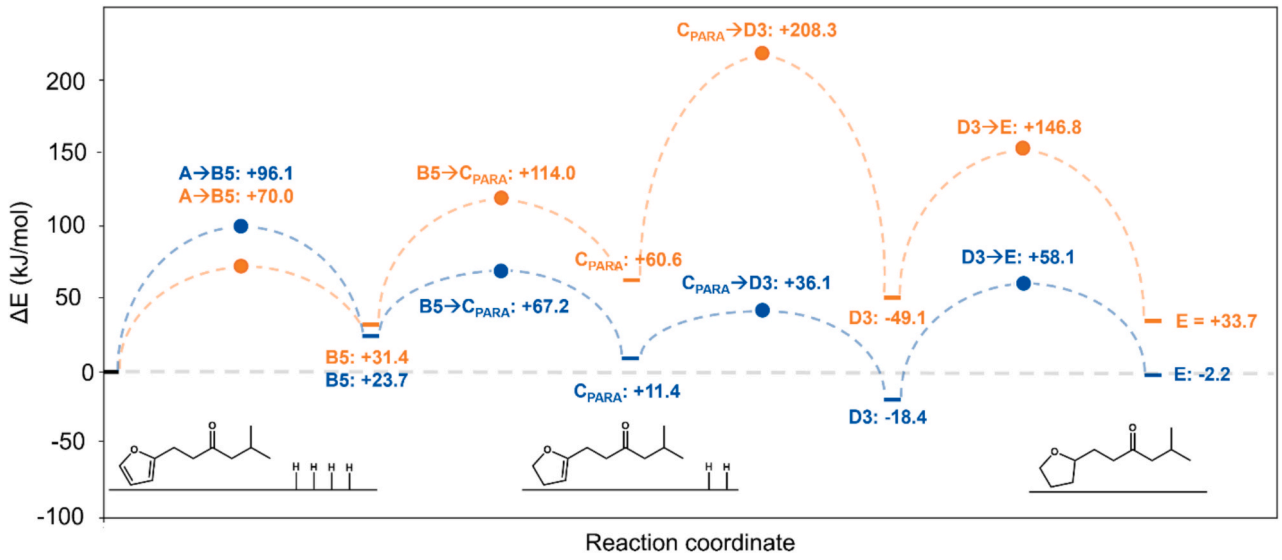

Fig. 7. Energy profile for *para* hydrogenation of ALD-2 over Pd(111) (blue) and Pt(111) (orange). Transition states between minima are marked with colored circles. Inset are the schematic representations of ALD-2 co-adsorbed with four H adatoms (left) and adsorbed ALD-3 (right). Relative energies are in kJ/mol. (For interpretation of the references to colour in this figure legend, the reader is referred to the web version of this article.)

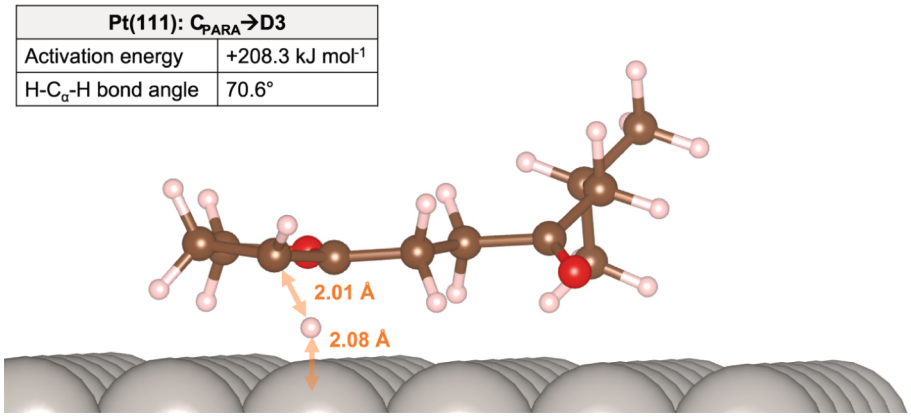

Fig. 8. Optimized transition state structure for the hydrogenation of the *para* product to the intermediate D3 over Pt(111). Color scheme as in previous figures.

noted that if hydrogenation of the *para* product first takes place at carbon-2 (C_{PARA} → D2), the resultant activation energies for Pd(111) (E_A = +314.1 kJ mol^{-1}) and Pt(111) (E_A = +326.0 kJ mol^{-1}) become rather insurmountable in mild conditions. The transition state corresponding to the hydrogenation of carbon-3 over Pt(111) (C_{PARA} → D3) is given in Fig. 8. The migration of the H atom to the ring carbon is hindered by an unfavorable angle of approach (70.6°), as well as the large interatomic distance between carbon-2 (2.01 Å) and the catalyst surface (2.08 Å).

As shown in Fig. 9a, carbon-2 (q = +0.21 e) displays the highest partial positive charge of all the ring carbons in the gas phase due to its vicinity to an electronegative O atom at the 1-position. Over Pd(111) and Pt(111), all of the ring carbons become more positively charged due to electrons in the π-system being donated into the d-orbitals of the surface metal atoms. Unlike the chain C═C bond of ALD-1, the catalyst choice has a marked effect on the polarization of ALD-2′s ring carbons. Over Pt, all the ring carbons become more positively charged; particularly, carbon-2 (Δq = +0.07 e) and carbon-3 (Δq = +0.08 e). The decrease in the degree of π-conjugation likely destabilizes ALD-2 and its ring hydrogenation intermediates over Pt(111), as the ring system will distort to accommodate the unequal distribution of electrons.

The data in Table S2 suggest that *ortho* hydrogenation is a "selectivity bottleneck" that must be surpassed if the reduction of ALD-2's ring system is to be thermodynamically feasible. If carbon-3 is hydrogenated first, even more electron density is siphoned away from the ring system, further destabilizing the ring.

The extent to which positive charge accumulates at carbon-2 during *ortho* hydrogenation was assessed by conducting a final round of DDEC6 charge analysis on the B2 → C and B3 → C transition states. Over both Pd (111) and Pt(111) (Fig. 10a and c), hydrogenation at the 2-position leads to a significant reduction in the localized positive charge. This situation is greatly exacerbated over Pd(111) when carbon-3 is first hydrogenated (Fig. 10b), leading to the generation of a highly positive partial charge (q = +0.35 e) on carbon-2. Over Pt(111), a transition state for B3 → C hydrogenation (Fig. 10d) can be identified with an effectively unchanged carbon-2 partial charge from ALD-2 (Δq = –0.01 e), but this preservation of further charge accumulation comes at the cost of significantly distorting the bonds connecting carbon-2 to carbon-5 and the hydrogenated α,β-chain ($\angle$ = 128.3°). This disparity in the localization of the positive charge explains why the activation energy for B3 → C is significantly higher than the corresponding activation energy for B2 → C over both Pd(111) and Pt(111). For both catalysts, the optimal thermodynamic path begins with the initial hydrogenation of carbon-2, which minimizes the accumulation of a point-positive charge and

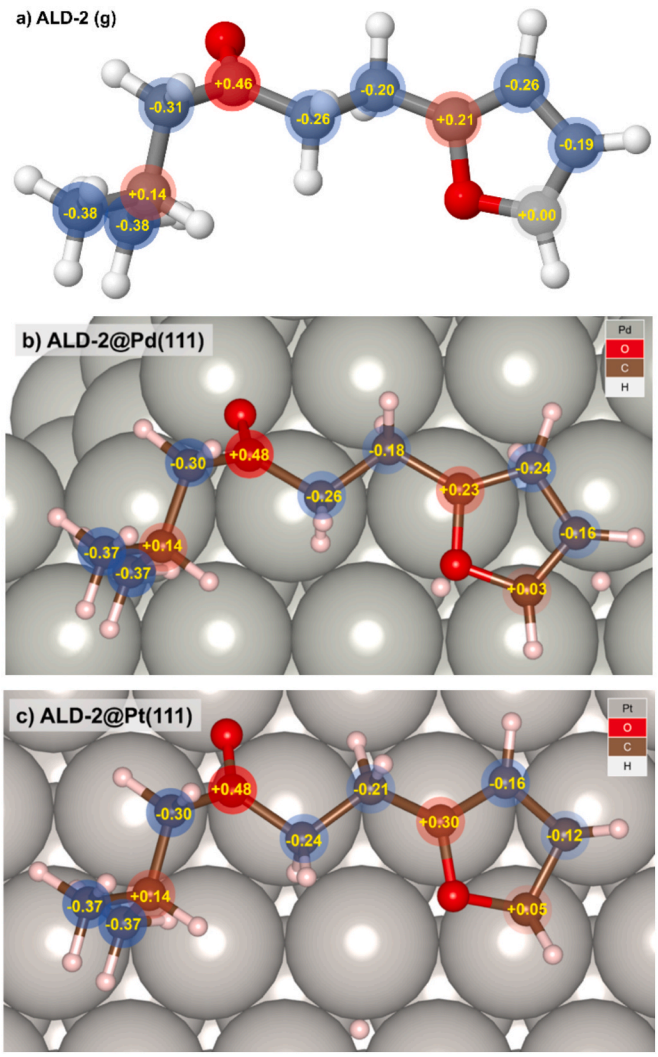

Fig. 9. DDEC6 charge analysis of ALD-2 (a) in the gas phase and adsorbed to (b) Pd(111) and (c) Pt(111). Carbon atoms with partial positive and negative charges are highlighted in red and blue, respectively. Figures given in units of elementary charge. (For interpretation of the references to colour in this figure legend, the reader is referred to the web version of this article.)

subsequent destabilization of the furan ring.

3.3. Overall hydrogenation path

A profile of the minimum energy path for the total hydrogenation of ALD-1 to ALD-3 is provided in Fig. 11. A complete table of energies for each step of this profile is provided in Table S3. Our calculations reveal a clear preference for *ortho* hydrogenation over both Pd and Pt, indicating that the poor selectivity of Pt-catalysis towards ring hydrogenation is due to steep energetic penalties associated with the accumulation of a positive charge on the ring carbons. Following the adsorption of molecular hydrogen from the gas phase, a stark contrast can be observed in the desorption energies of ALD-2 over Pd(111) ($\Delta E = +246.4$ kJ mol^{-1}) and Pt(111) ($\Delta E = +192.8$ kJ mol^{-1}). As the addition of the D3 (0) dispersion correction has been shown to introduce mild overbinding, the true desorption energies over both catalysts are likely lower than DFT would suggest. It should be highlighted that elementary steps corresponding to adsorption and desorption are those with the largest potential for error under the current computational scheme. However, the sheer disparity in ALD-2's adsorption energies suggests that premature desorption over Pt(111) contributes to its diminished selectivity towards ring hydrogenation.

3.4. Experimental validation

We measured the reaction kinetics for ALD-1 hydrogenation over Pd/Al_2O_3 and Pt/Al_2O_3 at 180 °C. The average particle sizes of Pd and Pt nanoparticles were 4.3 and 2.3 nm, respectively (Figs. S1 and S2), corresponding to metal dispersions of 26% and 49%. Before reaction, the catalysts were pre-reduced at 200 °C for 4 h. Under these conditions, Pd/Al_2O_3 was fully reduced, whereas for Pt/Al_2O_3, only Pt species weakly interacting with the alumina support were intentionally reduced, as evidenced by the H_2-TPR profiles (Fig. S3).

As inferred by GC–MS analysis (Fig. S4), ALD-1 hydrogenation over Pd/Al_2O_3 yields ALD-2 and ALD-3 as the primary products. ALD-1 is rapidly hydrogenated over Pd/Al_2O_3 and is fully consumed after 5 min (Fig. 12a). ALD-2 is the dominant product during the first 30 min, but it fast converted into ALD-3, showing reaching a yield of 7% after 1 h and 100% selectivity after 2 h. ALD-3 remains stable under reaction conditions for at least 18 h.

In contrast, the reaction proceeds more slowly over Pt/Al_2O_3, in agreement with the higher activation energies predicted by DFT. The time evolution of products over Pt/Al_2O_3 reveals two distinct kinetic regimes (Fig. 12b). During the initial stage of the reaction, significant amounts of ALD-3 are formed within the first few minutes, at levels comparable to those observed over Pd/Al_2O_3. Full ALD-1 conversion is achieved after 1 h, and after 2 h, the yields of ALD-2 and ALD-3 reach 55% and 45%, respectively. This rapid initial formation of ALD-3 indicates that furan ring hydrogenation is kinetically accessible on a relatively clean Pt surface, where ALD-2 can transiently adopt configurations favorable for ring hydrogenation. This rapid initial formation indicates that furan ring hydrogenation is kinetically accessible on a relatively clean Pt surface, where ALD-2 can transiently adopt configurations favorable for ring hydrogenation. These observations confirm the predictions from the calculations and are in good keeping with previous observations [48].

At longer reaction times, however, the net formation of ALD-3 is suppressed, and the yields of ALD-2 and ALD-3 evolve non-monotonically despite the reaction being conducted under excess H_2. In particular, the increase in ALD-2 yield accompanied by a decrease in ALD-3 yield between 2 and 3 h after reaching full ALD-1 conversion does not indicate gas-phase back-dehydrogenation of ALD-3, which would be thermodynamically unfavorable under excess H_2. Instead, this behavior is consistent with surface-mediated interconversion between adsorbed ALD-2*and ALD-3* in the presence of adsorbed hydrogen (H*).

It is well established from surface science and catalytic hydrogenation studies that, on Pt surfaces, adsorbed hydrogen can mediate reversible hydrogen-transfer steps, including β-hydride elimination and reinsertion, enabling interconversion between partially hydrogenated and more hydrogenated adsorbates without desorption into the gas phase [80,81]. Such behavior has been demonstrated for alkene/alkane systems on Pt(111), where stepwise hydrogen addition and removal occur through surface hydrogen shuttling, and for biomass-derived furanics, where surface hydrogen coverage strongly alters the distribution of hydrogenation and hydrogenolysis pathways [77]. In this context, matching our DFT results (Fig. 11), ALD-3* can undergo surface rearrangement or partial hydrogen transfer to regenerate ALD-2*, particularly on Pt surfaces where ring hydrogenation is associated with significant charge accumulation and weaker adsorption.

This interpretation is fully consistent with our DFT results, which show that while chain hydrogenation barriers are low on Pt(111), ring hydrogenation is associated with substantially higher activation energies and significant positive charge accumulation on the furan ring carbons. These electronic effects destabilize ring-hydrogenated intermediates and weaken their adsorption on Pt relative to Pd, favoring a dynamic surface equilibrium rather than sustained net conversion to ALD-3. Consequently, the early-time formation of ALD-3 reflects

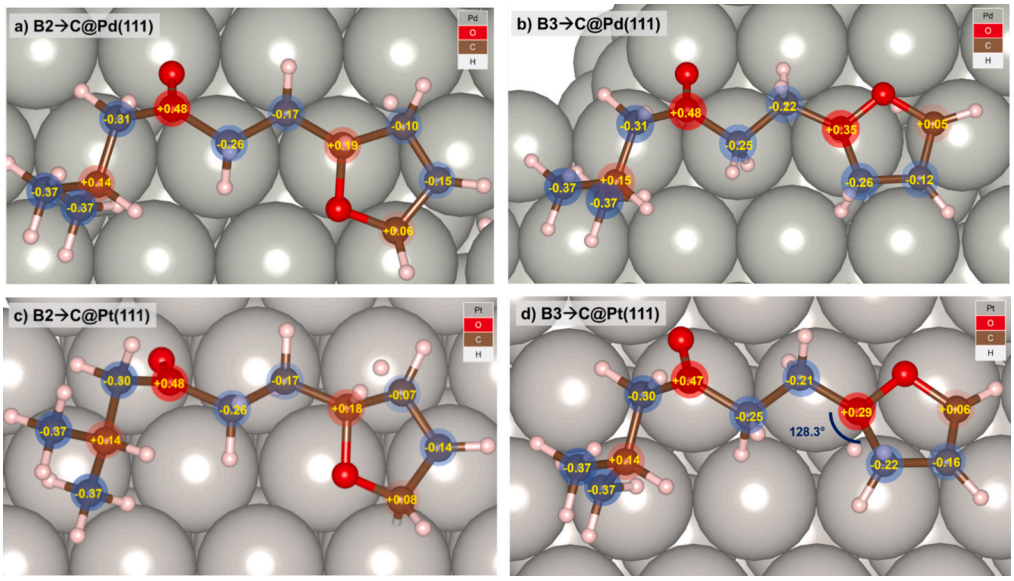

Fig. 10. DDEC6 charge analysis of a selection of *ortho* hydrogenation transition states: (a) B2 → C@Pd(111); (b) B3 → C@Pd(111); (c) B2 → C@Pt(111); (d) B3 → C@Pt(111). Carbon atoms with partial positive and negative charges are highlighted in red and blue, respectively. Figures given in units of elementary charge. (For interpretation of the references to colour in this figure legend, the reader is referred to the web version of this article.)

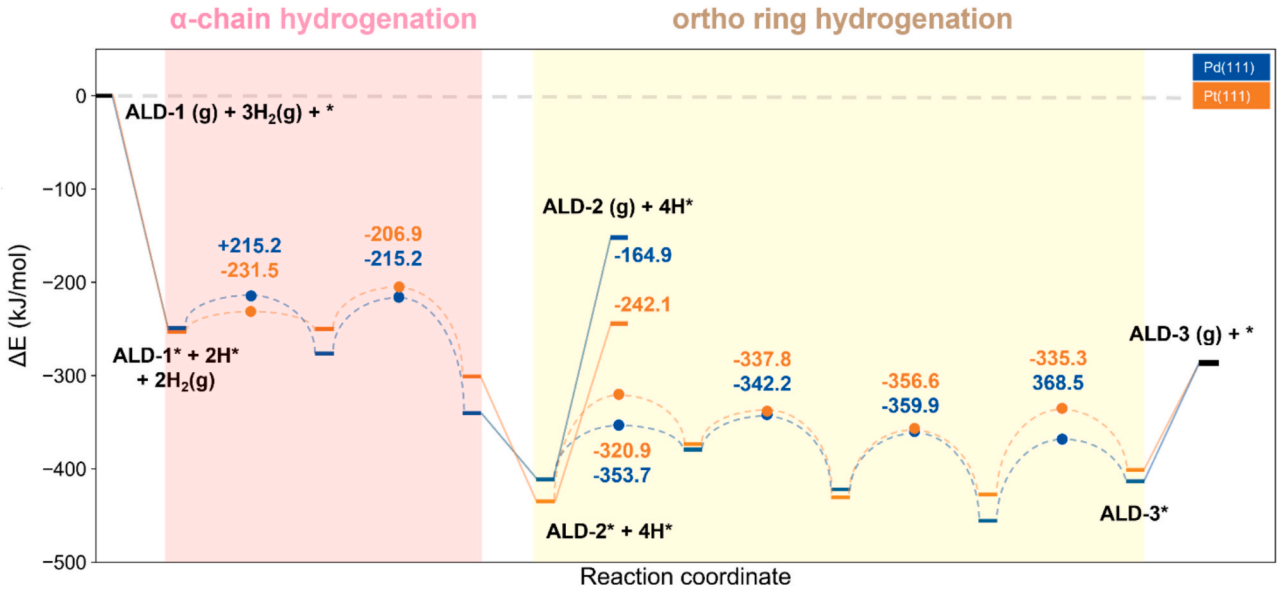

Fig. 11. Minimum energy path for the hydrogenation of ALD-1 to ALD-3 over Pd(111) and Pt(111). After binding to the catalyst in the gas phase, ALD-1 undergoes α-chain hydrogenation (pink) to ALD-2, and *ortho* ring hydrogenation (cream) to ALD-3. All dissociated hydrogens (H*) are bound at hollow sites. Transition states between minima are marked with colored circles. (For interpretation of the references to colour in this figure legend, the reader is referred to the web version of this article.)

kinetically accessible pathways on a clean surface, whereas the long-time behavior is governed by coverage- and charge-controlled limitations intrinsic to Pt, leading to the unusual but mechanistically meaningful kinetic profile observed experimentally.

When the reaction was allowed to proceed for extended times, additional transformations became apparent. After 18 h on stream, the yields of both ALD-2 and ALD-3 declined sharply over Pt/Al_2O_3, reaching final values of 33% and 12%, respectively, accompanied by a decrease in the carbon balance from ~100% to 33%. GC–MS analysis of the reaction mixture after 18 h (Fig. S5) revealed the formation of several higher-molecular-weight and cleavage products, including (E)-1-(furan-2-yl)hex-1-en-3-ol and 1-(furan-2-yl)hexan-3-ol, as well as methyl-cleaved products such as 1-(furan-2-yl)hexan-3-one and 1-(furan-2-yl)hexan-3-ol, and the isopropyl-cleaved product 3-(furan-2-yl) propanal. The formation of these by-products can originate from both ALD-2 and ALD-3 through subsequent hydrogenation, rearrangement, and C–C bond cleavage pathways involving the furan ring.

To investigate the potential effect of the support on the catalytic performance, additional experiments were conducted at 180 °C for 3 h over Pd/C and Pt/C (5 wt% nominal metal loading). The Pt/C catalysts exhibit weak metal-support interaction, with Pt reducibility in the range of 150–200 °C. Over Pd/C, ALD-2 and ALD-3 yields of 8% and 92% were obtained, respectively. In contrast, Pt/C produced 88% ALD-2 and only 7.5% ALD-3, respectively, indicating that Pt-catalyzed ring hydrogenation is even less favored over carbon supports than on alumina.

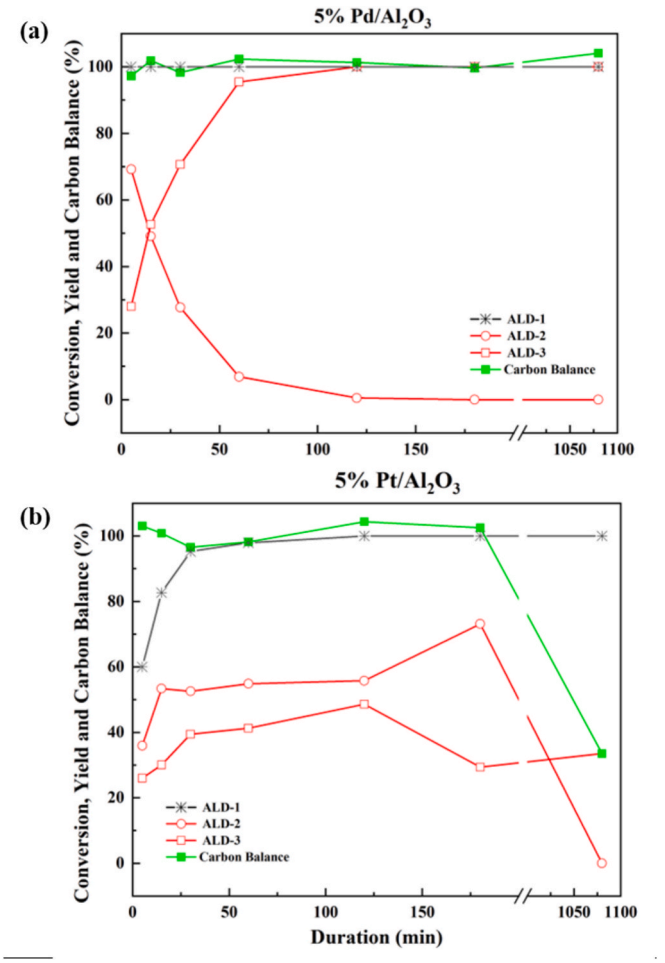

Fig. 12. Time-evolution of ALD-1 to the chain hydrogenation product ALD-2 and the fully hydrogenated ketone ALD-3 over (a) Pd/Al_2O_3 and (b) Pt/Al_2O_3. Reaction conditions: 180 °C, 20 bar H_2, 3.2 mmol ALD-1, 59.3 mmol MIBK, 66 mg catalyst. The catalysts were pre-reduced at 200 °C for 4 h before the reaction. The experiments were reproducible to within 5%.

4. Conclusions

Reaction profiles for the hydrogenation of ALD-1 over Pd(111) and Pt(111) were constructed using periodic DFT calculations within the RPBE-D3(0) framework and validated against kinetic experiments over supported Pd and Pt catalysts. In agreement with experimental observations, low-barrier pathways were identified for α-hydrogenation of the chain C═C bond on both metals, explaining the rapid and selective formation of ALD-2 irrespective of catalyst choice. DDEC6 population analysis reveals that this selectivity is driven by a combination of charge localization on the α-carbon and sterically favorable transition-state geometries.

In contrast, hydrogenation of the furan ring is strongly metal dependent. Over Pd(111), ring hydrogenation proceeds with relatively low activation barriers and limited charge accumulation on the ring carbons, leading to strong adsorption of partially and fully hydrogenated intermediates and enabling efficient conversion of ALD-2 to ALD-3. Over Pt(111), however, ring hydrogenation is associated with substantially higher activation barriers and pronounced positive charge accumulation on the furan ring carbons. These electronic effects destabilize ring-hydrogenated intermediates and weaken their adsorption, resulting in poor intrinsic selectivity towards ALD-3.

The combined experimental-theoretical analysis provides a mechanistic explanation for the unusual, non-monotonic kinetic profiles observed over Pt-based catalysts. While early-stage formation of ALD-3 indicates that furan ring hydrogenation is kinetically accessible on a relatively clean Pt surface, the subsequent evolution of product yields reflects a dynamic surface equilibrium between ALD-2* and ALD-3* mediated by adsorbed hydrogen. This surface-mediated interconversion, rather than irreversible sequential hydrogenation, dominates once full ALD-1 conversion is achieved, leading to transient increases in ALD-2 yield at the expense of ALD-3 despite the presence of excess hydrogen. At longer reaction times, secondary hydrogenation, rearrangement, and C–C cleavage reactions further divert carbon away from the primary products, reducing carbon balances over Pt catalysts.

These findings highlight the central role of charge redistribution and adsorption strength in governing both activity and selectivity in the hydrogenation of furfural-derived molecules. In particular, the results demonstrate that catalytic performance cannot be inferred solely from initial hydrogenation rates, but must also account for the stability and reversibility of surface-bound intermediates under reaction conditions. More broadly, this work illustrates how site-specific charge descriptors derived from first-principles calculations can be used to rationalize (and ultimately predict) metal-dependent selectivity trends in the upgrading of biomass-derived oxygenates. Such insights provide a foundation for the rational design of catalysts with improved control over hydrogenation pathways in sustainable bio-based chemical transformations.

CRediT authorship contribution statement

Max Quayle: Writing – original draft, Investigation, Formal analysis. **Zhuoli Wu:** Writing – original draft, Investigation, Formal analysis. **Marc Pera-Titus:** Writing – review & editing, Supervision, Resources, Formal analysis. **Alberto Roldan:** Writing – review & editing, Validation, Supervision, Project administration, Investigation, Funding acquisition, Formal analysis.

Declaration of competing interest

The authors declare the following financial interests/personal relationships which may be considered as potential competing interests: Alberto Roldan reports financial support was provided by Cardiff University. If there are other authors, they declare that they have no known competing financial interests or personal relationships that could have appeared to influence the work reported in this paper.

Acknowledgments

The authors acknowledge financial support from the EPSRC-funded UK Interdisciplinary Centre for Circular Chemical Economy (NIC3E) (EP/V011863/1). M. Quayle gratefully acknowledges the Isle of Man Department of Education, Sport, and Culture (DESC) for funding this work as part of his PhD. Z. Wu thanks Cardiff University and the European Research Council (ERC) for funding and support throughout her PhD. M. Quayle and A. Roldan extend their gratitude to G.A. Bramley and D.J. Willock for their helpful suggestions relating to charge analysis. Via our membership of the UK's HEC Materials Chemistry Consortium, funded by the EPSRC (EP/R029431), this work used the UK Materials and Molecular Modelling Hub for computational resources, which is partially funded by the EPSRC (EP/T022213). We also thank the EPRSC (EP/V029797/2) for their support relating to electron microscopy. For computational support, we thank the Isambard UK National Tier-2 HPC Service (https://gw4.ac.uk/isambard), operated by GW4 and the UK Met Office, and funded by the EPSRC (EP/P020224/1). Finally, we thank Supercomputing Wales for access to the Hawk HPC facility, partly funded by the European Regional Development Fund (ERDF). The datasets for this paper are publicly available via Figshare (https://figshare.com/s/cea295a78a9ec72f209f).

Appendix A. Supplementary data

Supplementary data to this article can be found online at https://doi.org/10.1016/j.jcat.2026.116774.

Data availability

The datasets for this paper are publicly available via Figshare (https://figshare.com/s/cea295a78a9ec72f209f).

References

[1] H.J. Brownlee, C.S. Miner, Industrial development of furfural, Ind. Eng. Chem. 40 (2) (1948) 201–204, https://doi.org/10.1021/ie50458a005.

[2] B.C.D. Hurd, A.R. Goldsby, Furan reactions. II. Furan from furfural, J. Am. Chem. Soc. 1932 (54) (1926) 2532–2536.

[3] C.J. Barrett, J.N. Chheda, G.W. Huber, J.A. Dumesic, Single-reactor process for sequential aldol-condensation and hydrogenation of biomass-derived compounds in water, Appl. Catal. B Environ. 66 (1–2) (2006) 111–118, https://doi.org/10.1016/j.apcatb.2006.03.001.

[4] W. Dedsuksophon, K. Faungnawakij, V. Champreda, N. Laosiripojana, Hydrolysis/dehydration/aldol-condensation/hydrogenation of lignocellulosic biomass and biomass-derived carbohydrates in the presence of Pd/WO_3–ZrO_2 in a single reactor, Bioresour. Technol. 102 (2) (2011) 2040–2046, https://doi.org/10.1016/j.biortech.2010.09.073.

[5] C. Li, D. Ding, Q. Xia, X. Liu, Y. Wang, Conversion of raw lignocellulosic biomass into branched long-chain alkanes through three tandem steps, ChemSusChem 9 (13) (2016) 1712–1718, https://doi.org/10.1002/cssc.201600386.

[6] L. Faba, E. Díaz, S. Ordóñez, Performance of bifunctional Pd/M_xN_yO (M = Mg, Ca; N = Zr, Al) catalysts for aldolization–hydrogenation of furfural–acetone mixtures, Catal. Today 164 (1) (2011) 451–456, https://doi.org/10.1016/j.cattod.2010.11.032.

[7] M. Gu, Q. Xia, X. Liu, Y. Guo, Y. Wang, Synthesis of renewable lubricant alkanes from biomass-derived platform chemicals, ChemSusChem 10 (20) (2017) 4102–4108, https://doi.org/10.1002/cssc.201701200.

[8] J. Yang, N. Li, G. Li, W. Wang, A. Wang, X. Wang, Y. Cong, T. Zhang, Solvent-free synthesis of C10 and C11 branched alkanes from furfural and methyl isobutyl ketone, ChemSusChem 6 (7) (2013) 1149–1152, https://doi.org/10.1002/cssc.201300318.

[9] M. Li, X. Xu, Y. Gong, Z. Wei, Z. Hou, H. Li, Y. Wang, Ultrafinely dispersed Pd nanoparticles on a CN@MgO hybrid as a bifunctional catalyst for upgrading bioderived compounds, Green Chem. 16 (9) (2014) 4371–4377, https://doi.org/10.1039/C4GC00850B.

[10] L. Faba, E. Díaz, S. Ordóñez, One-pot aldol condensation and hydrodeoxygenation of biomass-derived carbonyl compounds for biodiesel synthesis, ChemSusChem 7 (10) (2014) 2816–2820, https://doi.org/10.1002/cssc.201402236.

[11] R. Bielski, G. Grynkiewicz, Furan platform chemicals beyond fuels and plastics, Green Chem. 23 (19) (2021) 7458–7487, https://doi.org/10.1039/d1gc02402g.

[12] J.J. Pacheco, M.E. Davis, Synthesis of terephthalic acid via diels-alder reactions with ethylene and oxidized variants of 5-hydroxymethylfurfural, Proc. Natl. Acad. Sci. U. S. A. 111 (23) (2014) 8363–8367, https://doi.org/10.1073/pnas.1408345111.

[13] R. Noyori, T. Ohkuma, Asymmetric catalysis by architectural and functional molecular engineering: practical chemo- and stereoselective hydrogenation of ketones, Angew. Chem. - Int. Ed. 40 (1) (2001) 40–73.

[14] T. Ohkuma, M. Koizumi, M. Yoshida, R. Noyori, General asymmetric hydrogenation of hetero-aromatic ketones, Org. Lett. 2 (12) (2000) 1749–1751, https://doi.org/10.1021/ol0000814.

[15] Y. Lou, S. Marinkovic, B. Estrine, W. Qiang, G. Enderlin, Oxidation of furfural and furan derivatives to maleic acid in the presence of a simple catalyst system based on acetic acid and TS-1 and hydrogen peroxide, ACS Omega 5 (6) (2020) 2561–2568, https://doi.org/10.1021/acsomega.9b02141.

[16] O. Ershova, K. Nieminen, H. Sixta, The role of various chlorides on xylose conversion to furfural: experiments and kinetic modeling, ChemCatChem 9 (15) (2017) 3031–3040, https://doi.org/10.1002/cctc.201700269.

[17] K.J. Yong, T.Y. Wu, C.B.T.L. Lee, Z.J. Lee, Q. Liu, J.M. Jahim, Q. Zhou, L. Zhang, Furfural production from biomass residues: current technologies, challenges and future prospects, Biomass Bioenergy 161 (May) (2022) 106458, https://doi.org/10.1016/j.biombioe.2022.106458.

[18] X. Li, P. Jia, T. Wang, Furfural: a promising platform compound for sustainable production of C4 and C5 chemicals, ACS Catal. 6 (11) (2016) 7621–7640, https://doi.org/10.1021/acscatal.6b01838.

[19] D.T. Win, Furfural - gold from garbage, Au. J. Technol. 8 (4) (2005) 185–190.

[20] S. Wang, V. Vorotnikov, D.G. Vlachos, A DFT study of furan hydrogenation and ring opening on Pd(1 1 1), Green Chem. 16 (2) (2014) 736–747, https://doi.org/10.1039/c3gc41183d.

[21] G. Pruckmayr, P. Dreyfuss, Dreyfuss, M.P. Polyethers, Tetrahydrofuran and oxetane polymers, Kirk-Othmer Encycl. Chem Technol. (2000).

[22] L. Hu, L. Lin, S. Liu, Chemoselective hydrogenation of biomass-derived 5-hydroxymethylfurfural into the liquid biofuel 2,5-dimethylfuran, Ind. Eng. Chem. Res. 53 (24) (2014) 9969–9978, https://doi.org/10.1021/ie5013807.

[23] S. De, S. Dutta, B. Saha, One-pot conversions of lignocellulosic and algal biomass into liquid fuels, ChemSusChem 5 (9) (2012) 1826–1833, https://doi.org/10.1002/cssc.201200031.

[24] Á. Szabolcs, M. Molnár, G. Dibó, L.T. Mika, Microwave-assisted conversion of carbohydrates to levulinic acid: an essential step in biomass conversion, Green Chem. 15 (2) (2013) 439–445.

[25] M.A. Ravutsov, M.M. Marinova, A. Kurutos, S.P. Simeonov, Sources, sustainability and directions in the chemical synthesis of δ-aminolevulinic acid, Sustain. Chem. Pharm. 38 (2024) 101491, https://doi.org/10.1016/j.scp.2024.101491.

[26] I.Y. Eyüpoglu, M. Buchfelder, N.E. Savaskan, Surgical resection of malignant gliomas-role in optimizing patient outcome, Nat. Rev. Neurol. 9 (3) (2013) 141–151, https://doi.org/10.1038/nrneurol.2012.279.

[27] J. Slak, B. Pomeroy, A. Kostyniuk, M. Grilc, B. Likozar, A review of bio-refining process intensification in catalytic conversion reactions, separations and purifications of hydroxymethylfurfural (HMF) and furfural, Chem. Eng. J. 2022 (2021) 429, https://doi.org/10.1016/j.cej.2021.132325.

[28] G. Trapasso, G. Mazzi, B. Chícharo, M. Annatelli, D. Dalla Torre, F. Aricò, Multigram synthesis of pure HMF and BHMF, Org. Process Res. Dev. 26 (10) (2022) 2830–2838, https://doi.org/10.1021/acs.oprd.2c00196.

[29] N. Esmaeili, M.J. Zohuriaan-Mehr, H. Bouhendi, G. Bagheri-Marandi, HMF synthesis in aqueous and organic media under ultrasonication, microwave irradiation and conventional heating, Korean J. Chem. Eng. 33 (2016) 1964–1970.

[30] M. Musolino, J. Andraos, F. Aricò, An easy scalable approach to HMF employing DMC as reaction media: reaction optimization and comparative environmental assessment, ChemistrySelect 3 (8) (2018) 2359–2365.

[31] J. Zhu, G. Yin, Catalytic transformation of the furfural platform into difunctionalized monomers for polymer synthesis, ACS Catal. 11 (15) (2021) 10058–10083, https://doi.org/10.1021/acscatal.1c01989.

[32] S.E. Davis, L.R. Houk, E.C. Tamargo, A.K. Datye, R.J. Davis, Oxidation of 5-hydroxymethylfurfural over supported Pt, Pd and Au catalysts, Catal. Today 160 (1) (2011) 55–60, https://doi.org/10.1016/j.cattod.2010.06.004.

[33] M. Sajid, X. Zhao, D. Liu, Production of 2,5-furandicarboxylic acid (FDCA) from 5-hydroxymethylfurfural (HMF): recent progress focusing on the chemical-catalytic routes, Green Chem. 20 (24) (2018) 5427–5453, https://doi.org/10.1039/c8gc02680g.

[34] P. Sahu, A. Thorbole, R.K. Gupta, Polyesters using bioderived furandicarboxylic acid: recent advancement and challenges toward green PET, ACS Sustain. Chem. Eng. 12 (18) (2024) 6811–6826, https://doi.org/10.1021/acssuschemeng.4c01123.

[35] Y.N. Palai, A. Shrotri, A. Fukuoka, Selective oxidation of furfural to succinic acid over Lewis acidic Sn-beta, ACS Catal. 12 (6) (2022) 3534–3542, https://doi.org/10.1021/acscatal.1c05348.

[36] W. Zhu, F. Tao, S. Chen, M. Li, Y. Yang, G. Lv, Efficient oxidative transformation of furfural into succinic acid over acidic metal-free graphene oxide, ACS Sustain. Chem. Eng. 7 (1) (2019) 296–305, https://doi.org/10.1021/acssuschemeng.8b03373.

[37] M. Lomelí-Rodríguez, J.R. Corpas-Martínez, S. Willis, R. Mulholland, J.A. Lopez-Sanchez, Synthesis and characterization of renewable polyester coil coatings from biomass-derived isosorbide, FDCA, 1,5-pentanediol, succinic acid, and 1,3-propanediol, Polymers 10 (6) (2018) 1–19, https://doi.org/10.3390/polym10060600.

[38] M. Lomelí-Rodríguez, M. Martín-Molina, M. Jiménez-Pardo, Z. Nasim-Afzal, S. I. Cauët, T.E. Davies, M. Rivera-Toledo, J.A. Lopez-Sanchez, Synthesis and kinetic modeling of biomass-derived renewable polyesters, J. Polym. Sci. Part Polym. Chem. 54 (18) (2016) 2876–2887, https://doi.org/10.1002/pola.28173.

[39] E. De Jong, M.A. Dam, L. Sipos, G.J.M. Gruter, Furandicarboxylic acid (FDCA), a versatile building block for a very interesting class of polyesters, ACS Symp. Ser. 1105 (2012) 1–13, https://doi.org/10.1021/bk-2012-1105.ch001.

[40] A.J.J.E. Eerhart, A.P.C. Faaij, M.K. Patel, Replacing fossil based PET with biobased PEF; process analysis, energy and GHG balance, Energy Environ. Sci. 5 (4) (2012) 6407–6422, https://doi.org/10.1039/c2ee02480b.

[41] A. García-Ortiz, J.D. Vidal, M.J. Climent, P. Concepción, A. Corma, S. Iborra, Chemicals from biomass: selective synthesis of N-substituted furfuryl amines by the one-pot direct reductive amination of furanic aldehydes, ACS Sustain. Chem. Eng. 7 (6) (2019) 6243–6250, https://doi.org/10.1021/acssuschemeng.8b06631.

[42] S. Jiang, C. Ma, E. Muller, M. Pera-Titus, F. Jérôme, K. De Oliveira Vigier, Selective synthesis of THF-derived amines from biomass-derived carbonyl compounds, ACS Catal. 9 (10) (2019) 8893–8902, https://doi.org/10.1021/acscatal.9b03413.

[43] R. Xing, V.A. Subrahmanyam, H. Olcay, W. Qi, G.P.van Walsum, H. Pendse, W. G. Huber, Production of jet and diesel fuel range alkanes from waste hemicellulose -derived aqueous solutions, Green Chem. 12 (11) (2010) 1933–1946, https://doi.org/10.1039/C0GC00263A.

[44] H. Chang, A. Hussain Motagamwala, W.G. Huber, A.J. Dumesic, Synthesis of biomass-derived feedstocks for the polymers and fuels industries from 5-(Hydroxymethyl)Furfural (HMF) and acetone, Green Chem. 21 (20) (2019) 5532–5540, https://doi.org/10.1039/C9GC01859J.

[45] B. Pholjaroen, N. Li, J. Yang, G. Li, W. Wang, A. Wang, Y. Cong, X. Wang, T. Zhang, Production of renewable jet fuel range branched alkanes with xylose and methyl isobutyl ketone, Ind. Eng. Chem. Res. 53 (35) (2014) 13618–13625, https://doi.org/10.1021/ie5016365.

[46] L. Gao, I. Miletto, C. Ivaldi, G. Paul, L. Marchese, S. Coluccia, F. Jiang, E. Gianotti, M. Pera-Titus, Rational design of bifunctional hierarchical Pd/SAPO-5 for the synthesis of tetrahydrofuran derivatives from furfural, J. Catal. 397 (2021) 75–89, https://doi.org/10.1016/j.jcat.2021.03.003.

[47] M.C. Hernández-Soto, A. Erigoni, C. Segarra, F. Rey, U. Díaz, E. Gianotti, I. Miletto, M. Pera-Titus, Bifunctional hybrid organosiliceous catalysts for aldol condensation

– hydrogenation tandem reactions of furfural in continuous-flow reactor, Appl. Catal. Gen. 643 (2022) 118710, https://doi.org/10.1016/j.apcata.2022.118710.
[48] S. Jiang, W. Ramdani, E. Muller, C. Ma, M. Pera-Titus, F. Jerôme, K. De Oliveira Vigiera, Direct catalytic conversion of furfural to furan-derived amines in the presence of Ru-based catalyst, ChemSusChem 13 (7) (2020) 1699–1704, https://doi.org/10.1002/cssc.202000003.
[49] L. Gao, Z. Jiang, I. Miletto, E. Gianotti, E. Rebmann, L. Baussaron, F. Jiang, M. Pera-Titus, Robust Pd/Al_2O_3 bifunctional catalyst for single reactor tandem synthesis of furan and tetrahydrofuran derivatives from furfural, Chem. Eng. J. 473 (2023) 145021, https://doi.org/10.1016/j.cej.2023.145021.
[50] E. Schmidt, A. Vargas, T. Mallat, A. Baiker, Shape-selective enantioselective hydrogenation on Pt nanoparticles, J. Am. Chem. Soc. 131 (34) (2009) 12358–12367, https://doi.org/10.1021/ja9043328.
[51] K. Sytwu, F. Hayee, T.C. Narayan, A.L. Koh, R. Sinclair, J.A. Dionne, Visualizing facet-dependent hydrogenation dynamics in individual palladium nanoparticles, Nano Lett. 18 (9) (2018) 5357–5363, https://doi.org/10.1021/acs.nanolett.8b00736.
[52] J. Lv, D. Wang, X. Guo, W. Ding, W. Yang, Selective hydrogenation of phenylacetylene over high-energy facets exposed nanotubular alumina supported palladium catalysts, Catal. Commun. 181 (2023) 106715, https://doi.org/10.1016/j.catcom.2023.106715.
[53] F. Zaera, The surface chemistry of metal-based hydrogenation catalysis, ACS Catal. 7 (8) (2017) 4947–4967, https://doi.org/10.1021/acscatal.7b01368.
[54] I. Kowalec, L. Kabalan, A. Catlow, A. Logsdail, A computational study of direct CO_2 hydrogenation to methanol on Pd surfaces, Phys. Chem. Chem. Phys. 24 (16) (2022) 9360–9373, https://doi.org/10.1039/D2CP01019D.
[55] Á. Logadóttir, J.K. Nørskov, Ammonia synthesis over a Ru(0001) surface studied by density functional calculations, J. Catal. 220 (2) (2003) 273–279, https://doi.org/10.1016/S0021-9517(03)00156-8.
[56] C. Kittel, Introduction to Solid State Physics, 8th ed., Wiley, New York, 2005.
[57] B. Coq, A. Tijani, F. Figuéras, Particle size effect on the kinetics of P-chloronitrobenzene hydrogenation over platinum/alumina catalysts, J. Mol. Catal. 68 (3) (1991) 331–345, https://doi.org/10.1016/0304-5102(91)80091-G.
[58] J. Hafner, G. Kresse. The Vienna Ab-Initio Simulation Program VASP: An Efficient and Versatile Tool for Studying the Structural, Dynamic, and Electronic Properties of Materials. *Properties of Complex Inorganic Solids*. Springer Boston, MA 1997, pp 69–82.
[59] B. Hammer, L.B. Hansen, J.K. Nørskov, Improved adsorption energetics within density-functional theory using revised Perdew-Burke-Ernzerhof functionals, Phys. Rev. B - Condens. Matter Mater. Phys. 59 (11) (1999) 7413–7421, https://doi.org/10.1103/PhysRevB.59.7413.
[60] S. Grimme, J. Antony, S. Ehrlich, H. Krieg, A consistent and accurate ab initio parametrization of density functional dispersion correction (DFT-D) for the 94 elements H-Pu, J. Chem. Phys. 132 (15) (2010) 154104.
[61] B. Liu, L. Cheng, L. Curtiss, J. Greeley, Effects of van Der Waals density functional corrections on trends in furfural adsorption and hydrogenation on close-packed transition metal surfaces, Surf. Sci. 622 (2014) 51–59, https://doi.org/10.1016/j.susc.2013.12.001.
[62] A.Z. Khan, J. Alitt, R. Germaney, I. Hamada, P.P. Wells, N. Dimitratos, C.R. A. Catlow, A. Villa, A. Chutia, A comparative study on the stability of the furfural molecule on the low index Ni, Pd and Pt surfaces, R. Soc. Open Sci. 9 (3) (2022) 211516, https://doi.org/10.1098/rsos.211516.
[63] N. Mardirossian, M. Head-Gordon, Thirty years of density functional theory in computational chemistry: an overview and extensive assessment of 200 density functionals, Mol. Phys. 115 (19) (2017) 2315–2372, https://doi.org/10.1080/00268976.2017.1333644.
[64] A. Castro-Alvarez, H. Carneros, D. Sánchez, J. Vilarrasa, Importance of the electron correlation and dispersion corrections in calculations involving enamines, hemiaminals, and aminals. comparison of B3LYP, M06-2X, MP2, and CCSD results with experimental data, J. Org. Chem. 80 (24) (2015) 11977–11985, https://doi.org/10.1021/acs.joc.5b01814.
[65] I.K.M. Yu, F. Deng, X. Chen, G. Cheng, Y. Liu, W. Zhang, J.A. Lercher, Impact of hydronium ions on the Pd-catalyzed furfural hydrogenation, Nat. Commun. 13 (1) (2022) 7154, https://doi.org/10.1038/s41467-022-34608-8.
[66] H.J. Monkhorst, J.D. Pack, Special points for brillouin-zone integrations, Phys. Rev. B 13 (12) (1976) 5188–5192, https://doi.org/10.1103/PhysRevB.13.5188.
[67] G. Kresse, D. Joubert, From ultrasoft pseudopotentials to the projector augmented-wave method, Phys. Rev. B - Condens. Matter Mater. Phys. 59 (3) (1999) 1758–1775, https://doi.org/10.1103/PhysRevB.59.1758.
[68] P.E. Blöchl, Projector augmented-wave method, Phys. Rev. B 50 (24) (1994) 17953–17979, https://doi.org/10.1103/PhysRevB.50.17953.
[69] N.G.G. Limas. *Improved Methods for Computing the Properties of Atoms in Materials*; New Mexico State University, 2017.
[70] A.T. Manz, Apples to apples comparison of standardized to unstandardized principal component analysis of methods that assign partial atomic charges in molecules, RSC Adv. 12 (49) (2022) 31617–31628, https://doi.org/10.1039/D2RA06349B.
[71] A.T. Manz, N. Gabaldon Limas, Introducing DDEC6 atomic population analysis: part 1. Charge partitioning theory and methodology, RSC Adv. 6 (53) (2016) 47771–47801, https://doi.org/10.1039/C6RA04656H.
[72] N. Gabaldon Limas, A.T. Manz, Introducing DDEC6 atomic population analysis: part 2. Computed results for a wide range of periodic and nonperiodic materials, RSC Adv. 6 (51) (2016) 45727–45747, https://doi.org/10.1039/C6RA05507A.
[73] T.A. Manz, D.S. Sholl, Improved atoms-in-molecule charge partitioning functional for simultaneously reproducing the electrostatic potential and chemical states in periodic and nonperiodic materials, J. Chem. Theory Comput. 8 (8) (2011) 2844–2867, https://doi.org/10.1021/ct3002199.
[74] T.A. Manz, D.S. Sholl, Chemically meaningful atomic charges that reproduce the electrostatic potential in periodic and nonperiodic materials, J. Chem. Theory Comput. 6 (8) (2010) 2455–2468, https://doi.org/10.1021/ct100125x.
[75] A. Heyden, A.T. Bell, F.J. Keil, Efficient methods for finding transition states in chemical reactions: comparison of improved dimer method and partitioned rational function optimization method, J. Chem. Phys. 123 (22) (2005) 224101, https://doi.org/10.1063/1.2104507.
[76] G. Henkelman, H. Jónsson, A dimer method for finding saddle points on high dimensional potential surfaces using only first derivatives, J. Chem. Phys. 111 (15) (1999) 7010–7022, https://doi.org/10.1063/1.480097.
[77] M.J. Taylor, L. Jiang, J. Reichert, A.C. Papageorgiou, S.K. Beaumont, K. Wilson, A. F. Lee, J.V. Barth, G. Kyriakou, Catalytic hydrogenation and hydrodeoxygenation of furfural over Pt(1 1 1): a model system for the rational design and operation of practical biomass conversion catalysts, J. Phys. Chem. C 121 (15) (2017) 8490–8497, https://doi.org/10.1021/acs.jpcc.7b01744.
[78] J. Akinola, C.T. Campbell, N. Singh, Effects of solvents on adsorption energies: a general bond-additivity model, J. Phys. Chem. C 125 (44) (2021) 24371–24380, https://doi.org/10.1021/acs.jpcc.1c06781.
[79] F. Jia, B. Zhang, Computational mechanism investigation of C=C bond hydrogenation catalyzed by rhodium hydride, ChemPhysChem 24 (3) (2023) 1–11, https://doi.org/10.1002/cphc.202200562.
[80] F. Zaera, On the mechanism for the hydrogenation of olefins on transition-metal surfaces: the chemistry of ethylene on Pt(1 1 1), Langmuir 12 (1) (1996) 88–94, https://doi.org/10.1021/la9407020.
[81] P. Ye, A.J. Gellman, Transition state for β-hydride elimination in alkyl groups on Pt (1 1 1), J. Phys. Chem. B 110 (19) (2006) 9660–9666, https://doi.org/10.1021/jp061047v.